Original Research Article

International journal of spray and combustion dynamics

International Journal of Spray and Combustion Dynamics
0(0) 1–19

DOI: 10.1177/1756827717717390
journals.sagepub.com/home/scd

SAGE

Modelling of combustion acoustics sources and their dynamics in the PRECCINSTA burner test case

Felix Grimm[1], Jürgen Dierke[2], Roland Ewert[2], Berthold Noll[1] and Manfred Aigner[1]

Abstract

A stochastic, hybrid computational fluid dynamics/computational combustion acoustics approach for combustion noise prediction is applied to the PRECCINSTA laboratory scale combustor (prediction and control of combustion instabilities in industrial gas turbines). The numerical method is validated for its ability to accurately reproduce broadband combustion noise levels from measurements. The approach is based on averaged flow field and turbulence statistics from computational fluid dynamics simulations. The three-dimensional fast random particle method for combustion noise prediction is employed for the modelling of time-resolved dynamics of sound sources and sound propagation via linearised Euler equations. A comprehensive analysis of simulated sound source dynamics is carried out in order to contribute to the understanding of combustion noise formation mechanisms. Therefrom gained knowledge can further on be incorporated for the investigation of onset of thermoacoustic phenomena. The method-inherent stochastic Langevin ansatz for the realisation of turbulence related source decay is analysed in terms of reproduction ability of local one- and two-point statistical input and therefore its applicability to complex test cases. Furthermore, input turbulence statistics are varied, in order to investigate the impact of turbulence on the resulting sound pressure spectra for a swirl stabilised, technically premixed combustor.

Keywords

Combustion noise, PRECCINSTA, computational combustion acoustics, computational fluid dynamics, Reynolds averaged Navier Stokes, fast random particle method for combustion noise prediction, stochastic sound source reconstruction

Date received: 29 September 2016; accepted: 2 June 2017

1 Introduction

In civil aviation, noise emission is a big issue for passengers, residential areas close to airports and the environment. There is a great need for a detailed understanding of noise generation and, consecutively, noise damping mechanisms. The extent of the problem becomes obvious by looking at passenger volumes in civil aviation of the past decade. In the period of 2001 to 2014, the global number of transported passengers increased by 80%. According to estimates, volumes will again double from now until 2028.[1]

From today's standpoint, there are still certain noise-producing components of air planes that are poorly understood. Those are mainly parts in the turbofan engines and their interaction with each other. Engine noise makes up the predominant fraction of aircraft sound emission.[2,3] Therein, combustion noise significantly contributes at low frequencies.[4] With the establishment of turbofan engines, exhaust jet noise was reduced by large bypass ratios and also by increased engine efficiency and in turn lower jet velocities. Furthermore, a lot of research effort was put into the understanding and reduction of fan noise. This situation further increases the relative importance of

[1]German Aerospace Center (DLR), Stuttgart, Germany
[2]German Aerospace Center (DLR), Braunschweig, Germany

Corresponding author:
Felix Grimm, German Aerospace Center (DLR), Institute of Combustion Technology, Computer Simulation, Pfaffenwaldring 38-40, 70569 Stuttgart, Germany.
Email: felix.grimm@dlr.de

combustion noise for overall engine noise levels. The recent direction of development to lean combustion technologies for low-emission engines tends to further promote combustion noise emission. Therefore, the understanding of combustion noise is an important research topic with expected increasing relevance in the future. Further on, a more detailed understanding of sound source formation and sound source location in technically relevant combustion systems can contribute to investigations dealing with the onset of thermoacoustic instabilities, which can significantly damage burner systems and rapidly increase pollutant emission.

From a phenomenological point of view, combustion noise can be subdivided into indirect and direct combustion noise. There are several mechanisms leading to indirect combustion noise formation. It can emerge, e.g. from convectively transported hot spots passing to the subsequent turbine stages or through sudden flow constrictions.[5–7] Further causes for indirect combustion noise formation can be vorticity fluctuations[8,9] or compositional inhomogeneities.[10] Leyko et al.[11] reason that indirect combustion noise can be dominant over direct noise, especially for higher combustor exit Mach numbers, as in installed applications.

In contrast to this, direct combustion noise is linked to fluctuating heat release in the reaction zone, due to the interaction of the flame with turbulence. Actually, there is no feasible approach for the separation of indirect and direct combustion noise emission from engines.[12] This is subject to prevailing studies.[13–15]

In the past, direct combustion noise was numerically investigated in many works.[16–25] However, the sound generation mechanism and the spectral outcome of combustion noise are still poorly understood. From a modelling point of view, certain assumptions are necessary regarding the dynamics of direct combustion noise formation. Two of the most popular are either assuming a spectral distribution of heat release, as employed by for example Hirsch et al.,[25] where model spectra from turbulence theory are used in order to describe acoustic source term dynamics.[26] Or, the correlation dynamics of combustion noise sources can be directly modelled, as for example by Liu and Echekki.[27] In order to tackle the issue of getting close to the physical correlation of combustion noise sources, they furthermore published a study on direct numerical simulation (DNS) data of V-flames.[28] In the presented paper, a two-point space–time correlation function is employed for combustion noise prediction, relying on local turbulent integral statistics in the acoustic near field.

As summarised by Tam,[12] there are some theoretical investigations addressing the characteristics of turbulent combustion noise. Kotake and Takamoto[29,30] and Rajaram and Lieuwen[31] investigated the spectral shape of open flame combustion noise, finding that it is independent of configuration parameters like burner size, turbulence levels and fuel composition. Mahan and Karchmer[32] observed similarity between open flame combustion noise and high-speed jet noise. Tam[12] applied his similarity spectra[33] to several combustion noise measurements, also finding reasonable agreement from a semi-empirical theory developed for high-speed jets. Tam et al.[34] investigated combustion noise from auxiliary power units, being able to fit experimental data to one particular similarity spectrum associated to large-scale turbulence.[33] Furthermore, Mathews and Rekos[35] and Ho and Doyle[36] studied the spectral shape of noise for turbofan engines and respectively found characteristic spectral curves which however differ from the similarity theory of Tam et al.[33] Nonetheless, no present study goes beyond empirical findings.

The understanding of sound generation mechanisms in combustion systems is important for the accurate modelling of combustion noise emissions and thermoacoustic phenomena, which – as mentioned previously – can cause structural damage and significantly increased pollutant emission. In principle, sources of combustion acoustics can be determined from fully or partially scale resolving simulations, which also allow for the capture of thermoacoustic phenomena. However, direct methods are computationally expensive. Therefore, hybrid computational fluid dynamics/ computational aero acoustics (CFD/CAA) approaches are an attractive alternative, since they provide a large potential for computational resource savings. Furthermore, analysing a problem with hybrid methods gives the possibility to apply specifically optimised methods to sub-problems[18] and allows for manifold analyses, although acoustic feedback phenomena cannot be directly resolved.

The approach of combustion noise modelling utilised in this work was derived by Mühlbauer et al.,[37] using the sound source reconstruction algorithm from Ewert.[38–41] It was named the hybrid random particle mesh approach for combustion noise prediction (RPM-CN).[42] The employed physical source term model was derived from first principles, using a fundamental pressure–density relation, leading to the linearised Euler energy equation with a right-hand side (RHS) forcing,[42] where the complete RHS source expression of the pressure–density relation was taken from Candel et al.[43] Their comprehensive source term formulation was condensed to a temperature-variance based, monopole source term expression.

In recent works, the RPM-CN approach was further developed by Grimm et al.[44–46] by making use of a more efficient but also particle-based sound source reconstruction approach, the Fast Random Particle Method (FRPM) from Ewert et al.,[47] leading to FRPM-CN, the fast random particle method for combustion noise prediction (FRPM-CN). Increased

algorithmic efficiency allowed for the extension of the method to full 3D sound source and sound propagation modelling.[46] Employing FRPM furthermore facilitated the numerical consideration of recirculation zones, which is necessary for combustion noise prediction in swirl stabilized combustion.[48,49] A laboratory scale combustor was investigated in preceding works at atmospheric conditions with FRPM-CN by Grimm et al.,[49] which showed mainly broadband combustion noise emission. Fairly good agreement between measurements and simulation of flow field, combustion and acoustics were achieved, whereas combustion noise levels were predicted accurately especially for low frequencies. The hybrid approach was compared with a direct simulation from a compressible projection ansatz. It was shown that the hybrid method was almost an order of magnitude more efficient than the direct approach in terms of computational times. However phenomena with feedback between flow field and acoustics could not be captured by the sequential FRPM-CN. Consecutively, the PRECCINSTA burner was numerically investigated for a partially premixed operation mode.[50] Good agreement between experiment and CFD simulation was found for flow field and combustion. Experimentally determined sound pressure spectra were well reproduced especially for higher frequencies and the characteristic shape of combustion noise in the encased, swirl stabilized configuration was nicely described.

In the present work, the PRECCINSTA test case is investigated with a more detailed focus on sound source reconstruction and sound source dynamics, as reconstructed by the hybrid, stochastic FRPM-CN. The employed stochastic Langevin ansatz for turbulence synthetisation[47,51] is tested in view of one- and two-points statistics reproduction ability. The issue of the quality of reproduction of – from CFD simulations prescribed – integral turbulence statistics, namely integral length- and timescales is critically discussed. As mentioned previously, in general there is still a lack in understanding the noise production mechanisms in turbulent combustion. By proposing a particular correlation function and the provision of detailed analysis of resulting sound source dynamics, a contribution towards the understanding of combustion noise production mechanism from a statistical point of view is provided.

Additionally, sensitivity of sound pressure spectra and their characteristics from a variation of turbulence input quantities is tested. It is shown that a fairly good reproduction of broadband sound emission evaluated from experiments can be achieved with unmodified statistical input from CFD Reynolds averaged Navier Stokes (RANS) statistics with at the same time satisfactory reproduction of turbulence statistics. A detailed investigation of combustion noise spectral shape in view of dependence on turbulence levels is provided in order to contribute to studies towards a universally describing theory on combustion noise, possibly based on similarity spectra.[12]

The paper is structured as follows: First, method and theoretical framework are introduced. Subsequently, the combustor test case is described as well as the configurations of CFD RANS and computational combustion acoustics (CCA) computations. An effectively realised source variance evaluated solely from CFD data serves as main criterion for source field location determination. Consecutively, the employed stochastic Langevin model for turbulence synthetisation and a sound source reconstruction approach are evaluated for their ability to reproduce prescribed averaged turbulence statistics. Finally, a parametric study based on a variation of integral turbulence input parameters is carried out, analysing the impact on combustion noise sound pressure spectra.

2 The framework for source-correlation-based modelling of noise spectra

In the presented work, a sound source reconstruction algorithm is used. It realises correlated forcing in an assumed source region based on local turbulence statistics. Therefore, at first, the choice of modelling approach is justified by introducing the idea of noise spectra expressed with correlated sound sources.

Statistical noise modelling can be based on acoustic analogies, which were introduced first by Lighthill in the 1950s.[52,53] The analogy concept describes the physical behaviour of sound generated by a forcing mechanism q and its propagation in a domain via certain characteristics, expressed by a wave equation operator $\mathcal{L}$ acting on the fluctuating acoustic pressure as the left-hand side field variable

$$\mathcal{L}p'(\boldsymbol{x}_1, t) = q(\boldsymbol{x}_1, t) \tag{1}$$

In other words, as explained for example by Ewert et al.,[47] it provides the connection between the pressure recorder position with vanishing source terms on the left-hand side and the near field forcing emerging from sound created aerodynamically or – as in the herein treated case – created by the interaction of chemistry and turbulence. The pressure at sound recorder positions can then be generally expressed as

$$p'(\boldsymbol{x}_1, t) = \frac{1}{2\pi} \int\int\int_{-\infty}^{\infty} \hat{G}_a(\boldsymbol{x}, \boldsymbol{x}_1, \omega) q(\boldsymbol{x}, t_1) \cdot \exp(-i\omega(t - t_1)) dt_1 \mathrm{d}\omega d^n x \tag{2}$$

$\hat{G}_a(\boldsymbol{x}, \boldsymbol{x}_1, \omega)$ is the harmonic Green's function of an adjoint set of equations[54] associated to the wave operator $\mathcal{L}$. It is dependent on the source position $\boldsymbol{x}$, an observer point $\boldsymbol{x}_1$ and the angular frequency ω. The concept described with equations (1) and (2) is illustrated in Figure 1.

The autocorrelation of acoustic pressure at an arbitrary observer position $\boldsymbol{x}_1$ is related to the power spectral density (PSD) via Fourier transform

$$\hat{S}(\boldsymbol{x}_1, \omega) = \int_{-\infty}^{\infty} \left\langle p'(\boldsymbol{x}_1, t)\, p'(\boldsymbol{x}_1, t+\tau) \right\rangle \exp(i\omega t) \mathrm{d}\tau \quad (3)$$

$\langle \ldots \rangle$ denotes ensemble averaging. With the employment of equation (2), the spectrum can be expressed in terms of near field source statistics for ergodic problems

$$\hat{S}(\boldsymbol{x}_1, \omega) = \int\int\int_{-\infty}^{\infty} \hat{G}_a^*(\boldsymbol{x}, \boldsymbol{x}_1, \omega) \hat{G}_a(\boldsymbol{x}+\boldsymbol{r}, \boldsymbol{x}_1, \omega) \cdot \left\langle q(\boldsymbol{x}, t_1) q(\boldsymbol{x}+\boldsymbol{r}, t_1+\tau) \right\rangle \exp(i\omega\tau) \mathrm{d}\tau d^n\boldsymbol{x} d^n\boldsymbol{r} \quad (4)$$

An important information can be extracted from equation (4): the cross-covariance is the only unknown for the determination of acoustic pressure spectra at arbitrary observer positions. The Green's functions are deterministically linked to the prescribed wave operator. They provide the basic equations' fundamental solution. The cross-correlation therefore is the component of interest. It is implicitly modelled by the herein used sound source reconstruction approach.

Equation (4) furthermore motivates noise modelling with two-point correlated sources. Their accurate depiction is the key issue for reliable simulation of noise levels in combustion acoustics applications. Therefore, one of the main aspects of the presented investigations is the detailed analysis of realisation of source field correlation statistics for a complex application case.

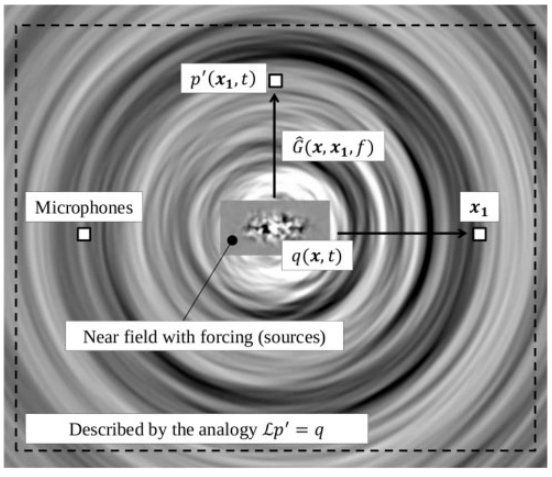

Figure 1. Illustration for equations (1) and (2), the concept of the acoustic analogy, near field forcing and the Greens function $\hat{G}$, connecting acoustic near field $\boldsymbol{x}$ and observer positions $\boldsymbol{x}_1$.

3 Stochastic combustion noise modelling

In the following section, the theoretical framework of the employed method, FRPM-CN, is described. The hybrid time-domain approach uses the sound source reconstruction algorithm FRPM from Ewert et al.[40,47] for the determination of statistically stationary, fluctuating sound sources $Q(\boldsymbol{x}, t)$ according to local turbulence and flow field statistics from CFD simulations.

3.1 The fast random particle method for combustion noise prediction

A main feature of the method is the accurate realisation of one and two-point statistics of the resulting fluctuating sound sources. Sources are constructed from an Eulerian point of view.[55,56] Their cross-covariance is Gaussian in space and exponential in time

$$\mathcal{R}(\boldsymbol{x}, \boldsymbol{r}, \tau) = \langle Q(\boldsymbol{x}, t) Q(\boldsymbol{x}+\boldsymbol{r}, t+\tau) \rangle = \hat{R}(\boldsymbol{x}) \exp\left(-\frac{|\tau|}{\tau_T} - \frac{\pi}{4 l_T^2(\boldsymbol{x})} |\boldsymbol{r} - \boldsymbol{u}_0^c \tau|^2 \right) \quad (5)$$

Equation (5) is the FRPM-method inherent correlation function. It is herein assumed to be approximately valid for the correlation function of monopole combustion noise sources in a turbulent flow regime. Up to now, the exact correlation function of combustion noise sources for swirl stabilised, partially premixed combustion is still not known. Therefore it has to be assumed and the assumption has to be validated.

l_T and τ_T denote integral length- and time-scales and u_0^c is the convection velocity. The convention with spatial variables is $\boldsymbol{x}$ for the source field location. $\boldsymbol{r}$ is the separation distance between sources on streamlines. $\hat{R}$ denotes the variance of the correlated quantity for no separation space $\boldsymbol{r}$ and time τ. The correlation function, as realised by equation (5), is depicted in Figure 2. It describes an exponential decay of sound sources, based on the local integral time scale. Spatial extensions of downstream correlation peaks depend on the local integral length scale. Their location on the time-delay axis results from source convection velocity along the investigated streamline. So to say, the correlation function as depicted in Figure 2 describes turbulence induced decay of sound sources along flow field streamlines and how sound sources develop while travelling downstream.

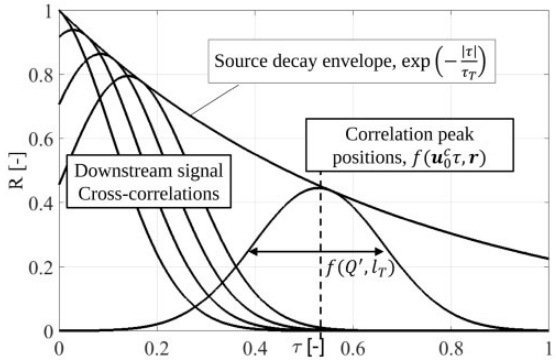

Figure 2. Employed space–time correlation function for combustion noise sources, according to equation (5). Time delay over normalised correlation coefficient.

The basic concept behind the employed sound source reconstruction algorithm is to obtain fluctuating sources by the spatial filtering of a spatial white noise field $\mathcal{U}$

$$Q(\boldsymbol{x}, t) = \int_{V_S^n} \hat{A}(\boldsymbol{x})\mathcal{G}(|\boldsymbol{x} - \boldsymbol{x}'|, l_T)\mathcal{U}(\boldsymbol{x}', t)d^n\boldsymbol{x}' \qquad (6)$$

$\mathcal{G}$ represents the filtering operation, which is for FRPM recursive.[47] The filter kernel width depends on the local integral length scale l_T. Integration is performed over the source domain V_S^n, n denotes the dimension. The amplitude function $\hat{A}(\boldsymbol{x})$ needs to be scaled in a way that it preserves the local target variance for $Q(\boldsymbol{x}, t)$.[57,47,42] It is connected with the source variance $\hat{R}$ through

$$\hat{A} = \sqrt{\hat{R}(\boldsymbol{x})/l_T^n(\boldsymbol{x})} \qquad (7)$$

Equation (6) is implemented with a particle concept, where particles i at positions x_i carry a random value, which is used for source reconstruction from filtering operations on the discrete spatial noise field $\mathcal{U}$. Source dynamics in a turbulent flow field are then modelled as follows: A decorrelation effect in time during particle convection is realised with an appropriate change of random values of particles. This is mathematically described with a Langevin equation.[51,47] It is shaped in a Lagrangian frame, reading

$$\frac{D_0}{Dt}\mathcal{U} = -\frac{1}{\tau_T}\mathcal{U} + \sqrt{\frac{2}{\tau_T}}\xi(\boldsymbol{x}, t) \qquad (8)$$

$D_0/Dt = \partial/\partial t + \boldsymbol{u}_0^c \cdot \nabla$ and the convection velocity are determined by the averaged velocity field $\boldsymbol{u}_0^c$ which is extracted from CFD simulations. $\xi(\boldsymbol{x}, t)$ represents spatio-temporal white noise with a Gaussian statistical distribution, for which the properties

$$\langle \xi(\boldsymbol{x}, t) \rangle = 0 \qquad (9)$$

$$\langle \xi(\boldsymbol{x}, t)\xi(\boldsymbol{x} + \boldsymbol{r}, t + \tau) \rangle = \delta(\tau)\delta(\boldsymbol{r}) \qquad (10)$$

hold. Equation (8) and its implications for the properties of $\xi(\boldsymbol{x}, t)$ and $\mathcal{U}(\boldsymbol{x}, t)$ account for the shape of the temporal part of the correlation function in equation (5), $\exp(|\tau|/\tau_T)$. The analytical solution for sound source decay according to equation (8) describes an exponential curve, which is also drawn in Figure 2. Details on the employed concept of convective white noise and its impact on the properties of $\xi(\boldsymbol{x}, t)$ and $\mathcal{U}(\boldsymbol{x}, t)$ are discussed in detail for example by Ewert et al.[47]

According to equation (6), a spatial filter is convoluted with the white noise field, leading to the spatial component of equation (5), as shown in foregoing works by Mühlbauer et al.[55,58] The spatial filters used in this work are Gaussian. The filter width is dependent on the local length scale, prescribed by the RANS flow field. The advancement of the random particle values in time and therefore the decorrelation mechanism is realised by discretising equation (8) with

$$r_i(t + \Delta t) = \alpha r_i(t) + \beta s_i(t) \qquad (11)$$

as explained in the literature.[40,47,58] A particle i carries a random value at time $t + \Delta t$, which is made up by $r_i(t)$ and $s_i(t)$ at time t, a Gaussian time-uncorrelated random value. This discrete approach realises the exponential decay or decorrelation for the appropriate choice of α and β, which are both related to the time scale τ_T via $\alpha = 1 - \Delta t/\tau_T$ and $\beta = (2\Delta t/\tau_T)^{1/2}$. β is chosen in a way to transiently preserve the RMS value of r_i. The overall sound source reconstruction procedure for a swirl-stabilised combustion test case is depicted in Figure 3.

Particles i are homogeneously seeded onto the source field, carrying random values r_i. Those values change at every time step according to equation (11), which is the implementation of the Langevin concept of equations (8) and (10). Source convection is incorporated by convecting particles with the underlying mean velocity field $\boldsymbol{u}_c$ from CFD simulations. The particle field is mapped to an orthonormal source field grid using area weighting. In that way, discrete noise is realised, which develops in time according to equation (8) or explicitly, equation (11). Spatial, recursive filtering (equation (6)) and amplitude scaling of source fluctuation with the local temperature variance solution from CFD simulations gives the physical realisation of broadband combustion noise sources.

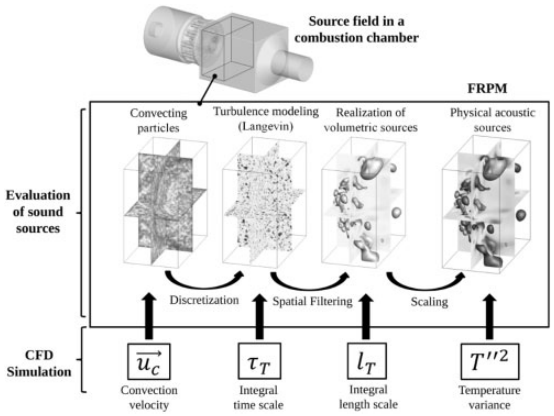

Figure 3. Scheme of the fast random particle method for a swirl-stabilised combustor application case. Steps to sound sources from a field of particles carrying random values.

3.2 Combustion noise source term formulation and the acoustic model

In the present work, a modified set of linearised Euler equations in combination with a temperature variance based source term formulation is used. Components with mean flow gradient terms are neglected. This denotes a compromise for more stability of the CCA simulations but against an exact depiction of refraction effects. The modified set reads

$$\frac{\partial \rho'}{\partial t} + \widetilde{\boldsymbol{u}} \cdot \nabla \rho' + \bar{\rho} \nabla \cdot \boldsymbol{u}' = 0 \tag{12}$$

$$\frac{\partial \boldsymbol{u}'}{\partial t} + (\widetilde{\boldsymbol{u}} \cdot \nabla)\boldsymbol{u}' + \frac{\nabla p'}{\bar{\rho}} = 0 \tag{13}$$

$$\frac{\partial p'}{\partial t} + \widetilde{\boldsymbol{u}} \cdot \nabla p' + \gamma \bar{p} \nabla \cdot \boldsymbol{u}' = q_p \tag{14}$$

The noise source model in conjunction with the linearised Euler equations was derived and presented in detail by Mühlbauer et al.[42] A pressure–density relation with a generalised formulation for RHS terms is reshaped in order to get the left-hand side equal to the energy equation of linearised Euler equations, expressed in terms of pressure. A RHS prescription rule for sound sources is there-from obtained, eventually leading to the compact source term formulation

$$q_p = \frac{\gamma \bar{p}}{\tilde{T}} \frac{\tilde{D} T''}{Dt} \tag{15}$$

$\gamma, \bar{p}$ and T are given as field variables from RANS calculations and they form the pre-factor for the reconstructed combustion noise sources. The $\sim$ denotes Favre-averaging. The substantial time derivative $\tilde{D}''/Dt$ in equation (15) is subject to FRPM reconstruction. Therefore, the variance and amplitude scaling according to equation (6) and equation (7) holds. The correlation function parameters in equation (5), namely the turbulent length- and time-scales l_T and τ_T, have to be specified

$$l_T = c_{T,l} \frac{k^{1/2}}{\beta^* \omega} \quad \text{and} \quad \tau_T = c_{T,\tau} \frac{1}{\beta^* \omega} \tag{16}$$

k and ω are the turbulent kinetic energy and turbulence frequency, respectively. $\beta^* = 0.09$ is a constant of the employed $k-\omega$–SST turbulence model.[59] The coupling parameters $c_{T,l}$ and $c_{T,\tau}$ of the integral scales in equation (16) are varied in parametric studies within this work to investigate a variation of statistical turbulence input on resulting sound pressure spectra. This variation also denotes a test of different correlation functions of combustion noise sound sources, since changes in correlation parameters alter the shape of the realised correlation function, equation (5). The variance scaling is formulated[42] for the temperature variance as the driving sound generation mechanism to

$$\hat{R} = \frac{\widetilde{T''2}}{\tau_T^2} \quad \text{and} \quad \hat{A} = \frac{1}{\tau_T} \sqrt{\frac{\widetilde{T''2}}{l_T^n}} \tag{17}$$

The temperature variance, however, is determined from a transport equation[60,58] in the preceding RANS calculations, as introduced in foregoing investigations,[44–46,48] reading

$$\begin{aligned} &\bar{\rho} \nabla \cdot (\widetilde{T''2}\boldsymbol{u}) - \nabla \cdot \left[\left(\frac{\mu}{Pr} + \frac{\mu_t}{Pr_t} \right) \nabla \widetilde{T''2} \right] \\ &= \underbrace{2 \frac{\mu_t}{Pr_t} (\nabla \tilde{T})^2}_{\text{production}} \underbrace{- \bar{\rho} C_T \frac{\widetilde{T''2}}{\tau_T}}_{\text{production}} \end{aligned} \tag{18}$$

with the model constant $C_T = 2$. μ and Pr are the viscosity and the Prandtl number, respectively. The indices t and T mean turbulent and turbulent temperature associated, respectively.

4 The PRECCINSTA burner test case

The basic design of the PRECCINSTA burner test case is schematically shown in Figure 4. An air plenum is mounted upstream of the combustion chamber. Air is led into the plenum and consecutively through a swirler into the combustor. The radially aligned swirler consists of 12 vanes. The fuel (CH_4) is induced from a fuel plenum into the swirler through single holes in a jet-in-crossflow alignment.[61] Fuel and air then mix within

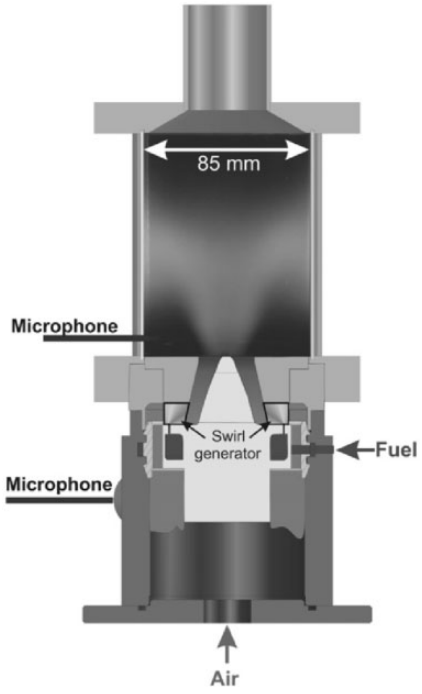

Figure 4. Schematic drawing of the PRECCINSTA burner with basic dimensions.[61]

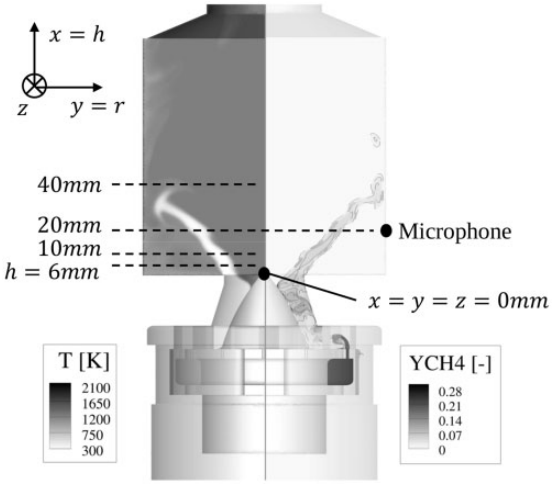

Figure 5. Sectional view of temperature (left) and methane mass fraction (right) in the combustor with measurement locations and spatial conventions.

a converging nozzle, which is characterised by a conical centre body. The tip of the centre body denotes the origin of the global coordinate system, as shown in Figure 5. Subsequently, the technically premixed air–fuel mixture expands into the combustion chamber, which has the dimensions $114 \times 85 \times 85$ mm. There, for the investigated operation condition, the flame anchors at the tip of the bluff body and shows a V-shape, as can be seen in Figure 5. The burnt gas exits the combustion chamber through a converging nozzle.

A CFD RANS simulation is compared with averaged results from stereoscopic particle image velocimetry (PIV)[61,62] of velocity at horizontal profile lines in the combustion chamber at $h = 6$ mm, 10 mm, 20 mm and 40 mm. Single-shot laser Raman measurements[61] are available for temperature profile lines and the mean species concentrations (O_2,CH_4,CO_2,H_2O) at the same positions for validation of combustion and reaction mechanism.

Acoustic pressure is sampled at a combustion chamber microphone position at $z = 42.5$ mm, $y = r = 42.5$ mm and $x = h = 20$ mm. Air and fuel mass flow rates are $\dot{m}_{\text{air}} = 574$ g/min and $\dot{m}_{\text{fuel}} = 30$ g/min at the respective inlets, while the burner is operated at $P_{th} = 25$ kW and $\Phi = 0.9$ with a global mixture fraction of $f = 0.0498$. Methane and air are burnt at atmospheric conditions. Under the given operation conditions, the Reynolds number of the configuration is $Re = 27{,}000$, evaluated at the plenum air inlet. The local Mach number at the air inlet is $Ma = 0.047$ and $Ma = 0.1$ at the combustor exhaust duct. The maximum Mach number is estimated to $Ma = 0.15$ in the nozzle prior to the combustion chamber expansion. Mach numbers are estimated based on the averaged CFD flow field quantities.

5 CFD simulation

The CFD simulation serves as basis for the consecutively performed combustion acoustics analyses. Mean flow field quantities are fed as background flow field to the linearised Euler equations for sound propagation. Besides that, flow field and turbulence statistics determine turbulence induced decay and local source extensions in the sound source reconstruction algorithm.

The CFD RANS setup was introduced in detail by Grimm et al.[50] and will therefore only be sketched here. Different discretisations and reaction mechanisms were tested by Grimm et al.[50] and a detailed discussion of results and an opposition with experimental data was provided. It was reasoned that the results are in good agreement with experimental data and therefore suitable for the reproduction of sound sources and prediction of measured power spectral densities in the treated model combustor. Consequently, numerical CFD results are not explicitly shown here.

Simulations are carried out with the finite-volume-based German Aerospace Center (DLR) in-house code THETA in its incompressible variant. The incompressible governing equations are treated with a SIMPLE solution strategy. For solution progression in time, a three-point backward (TPB) scheme is employed. Turbulence is modelled with the k-ω–shear stress

transport (SST) model in its version of 2003.[59] The computational grid consists of 16.6 M tetrahedral elements and 2.9 M points. It is refined in the regions of the swirler, the converging nozzle, the main reaction zone in the combustion chamber and contains prism layers in the converging nozzle leading to the combustion chamber expansion. At inlets, mass flow rates are specified, while the static pressure is set to ambient reference conditions at the combustion chamber outlet.

Combustion is modelled with a global one-step reaction scheme of Westbrook and Dryer[63] in a combined Eddy Dissipation Model/ Finite Rate Chemistry (EDM/FRC) approach. For a field solution of temperature variance in steady state calculations, an additional transport equation for the temperature variance, equation (18), is solved on top of the reacting flow field solution.

6 CCA specifications

Acoustics simulations are performed with the DLR in-house finite-difference based code perturbation investigation of aerodynamic noise (PIANO)[64] and sound source reconstruction is carried out with FRPM. Due to the use of a finite-difference based scheme, the computational grid is required to be fully structured. It consists of 1.5 M hexahedral elements and 1.94 M nodes in 938 blocks. For spatial discretisation, the DRP scheme of Tam and Webb[65] is used. Up to 15 kHz are spatially resolved. Resolution is highest in regions with large flow field and density gradients, while smallest resolution is given in the upstream air plenum. Furthermore, especially in large density gradient regions, the computational grid is optimised with respect to the local maximum cell growth rate, realising a value of 1.05 for adjacent cells. For time evolution, a four-step Runge–Kutta scheme is used. Mean flow field quantities are interpolated onto the computational acoustics grid from the unstructured CFD mesh using a statistical Kriging algorithm.[66] The density field is smoothed in the regions where the fuel jets enter the air stream in the swirler ducts for stability reasons. Besides this local smoothing, the background flow field from CFD remains unmodified. The overall simulation time step is $\Delta t = 2.2 \times 10^{-7}$ s. Pressure spectra are evaluated over a simulated real-time of 0.2 s. The outer topology of the computational grid and employed boundary conditions are displayed in Figure 6.

For the combustor inlet, a non-reflecting radiation boundary[65] is applied. Only minor sound reflection from the plenum inlet is expected due to an area jump from inlet tube to plenum of about 3/10. Also, the inlet tube leading to the air plenum in the experiment is considerably longer ($L/D = 9$) compared to the simulation setup ($L/D = 1.04$), with the diameter of the

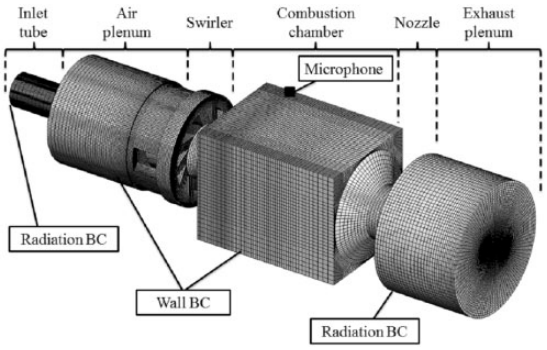

Figure 6. Computational combustion acoustics grid with employed boundary conditions.[50]

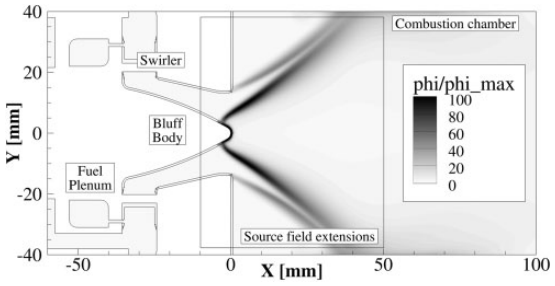

Figure 7. Combustor mid-plane with regions of contribution to the combustion noise source term. Effectively realised target source variance φ, evaluated from CFD RANS data and normalised to the maximum value in the inner shear layer φ_{max}.[50] CFD: computational fluid dynamics; RANS: Reynolds averaged Navier Stokes.

duct $D = 24$ mm. Therefore, inlet tube computational boundaries are treated as non-reflecting. The combustor outlet tube is enclosed by an additional plenum, surrounded with a sponge layer and radiation boundaries. Therefore, a natural wave reflection behaviour is enabled at the combustor outlet in the prevailing low Mach number case. Walls are set as fully reflecting with a ghost-point modelling ansatz from Tam and Dong.[67]

For the analysis of source region spatial extensions in the treated application case, the effectively realised target variance for no separation distance and time is evaluated from CFD-RANS quantities, reading

$$\varphi = \frac{\gamma \bar{p}}{\tilde{T}} \sqrt{\frac{\widetilde{T''2}}{\tau_T^2}} \tag{19}$$

All variables in equation (19) can be directly extracted from CFD RANS data. The resulting contour of φ/φ_{max} is shown on a combustor mid-plane cut in Figure 7. It indicates region in the combustion chamber where contributions to the combustion noise source term are present.

Based on the profile, the source field region extensions are chosen, including 95% of the source contributions. Strongest amplitudes of noise sources are according to this indicator present close to the stagnation point near the tip of the conical centre body in the inner shear layer. The contour furthermore indicates contributions in the outer shear layer, which are herein considered.

Based on the φ-criterion of equation (19), the source field region is chosen to be within $x \in [-10\text{mm}; 50\,\text{mm}]$ and $y, z \in [-38\,\text{mm}; 38\,\text{mm}]$. The auxiliary source field grid is discretised with 346.6 K elements and an initial particle distribution of 1.154 particles per cell. A recursive filter is employed for source filtering according to the local turbulent length scale for source extensions and turbulence induced decay is incorporated with the previously introduced first order Langevin ansatz. The FRPM grid is equidistant and orthogonal with a direct resolution of $\Delta x = \Delta y = \Delta z = 1\,\text{mm}$.

The analysis of source statistics reproduction ability with FRPM and the Langevin model is investigated for one- and two-point statistics. For one-point statistics analysis, the source signal is sampled at discrete points at heights of $h = x = 6, 10, 20, 40\,\text{mm}$ and RMS values of the fluctuating source signals are evaluated and compared to statistical input from CFD-RANS. For the two-point analysis, arrays of virtual microphones are placed along streamlines close to the inner shear layer of the CFD solution field, which are depicted in Figure 8. Recorded fluctuating source signal is auto- and cross-correlated.

Besides the performance of the stochastic sound source reconstruction approach, the impact of different turbulence levels on resulting pressure spectra in the combustion chamber is studied. The following sets of turbulence statistics input in Table 1 are tested, according to equation (16).

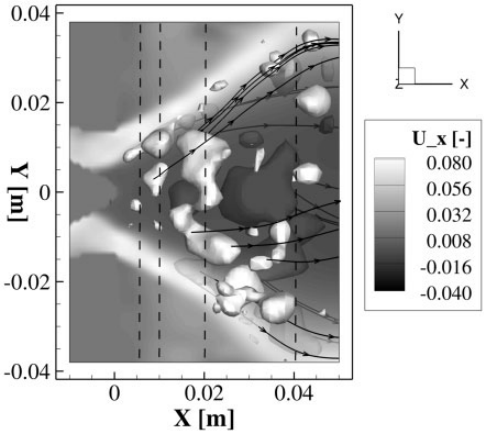

Figure 8. Source field with mid-plane of dimensionless axial velocity field, iso-contours of direct combustion noise sources and exemplary streamlines in the inner shear layer for correlation analysis of transient source signal. Dashed lines indicate sampling lines of fluctuating sound source signals at $h = x =$ 6, 10, 20, 40 mm for one-point statistics analysis.

7 CCA results

Selected results of the acoustics simulations are shown in Figure 9. Iso-surfaces of direct combustion noise sources are superimposed to mid-plane cuts of the reacting CFD RANS density distribution. It appears that direct combustion noise sources in this particular, partially premixed, swirl stabilised case, are mainly located in the inner shear layer in the combustion

Table 1. Investigated cases of turbulence input quantities according to equation (16) for the computational combustion acoustics simulations.

Case	c_{TI}	$c_{T,x}$	Case	c_{TI}	$c_{T,x}$
#1	0.001	1.0	#7	1.0	0.001
#2	0.01	1.0	#8	1.0	0.01
#3	0.1	1.0	#9	1.0	0.1
#4	0.5	1.0	#10	1.0	0.5
#5	1.5	1.0	#11	1.0	1.5
#6	2.0	1.0	#12	1.0	2.0

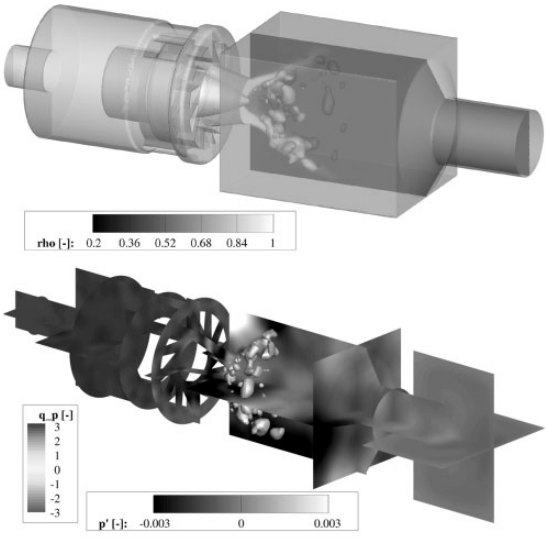

Figure 9. Top: CFD computational domain with mid-plane of normalized density $\bar{\rho}/(\rho_{\text{ref}})[-]$ distribution and exemplary iso-contours of combustion noise sound sources. Bottom: combustion chamber cutting planes with instantaneous solution of acoustic pressure $p'/(\rho_{\text{ref}} c_{\text{ref}}^2)[-]$ and iso-contours of direct combustion noise sources $q_p/(f_{\text{ref}} \rho_{\text{ref}} c_{\text{ref}}^2)[-]$. Reference quantities are listed in Appendix 1.
CFD: computational fluid dynamics.

chamber. Due to larger integral length scales further downstream, spatial extensions of sources increase accordingly.

However, largest amplitudes of source fluctuation are present rather close to the tip of the flame, as indicated with the effectively realised source variance in Figure 7. Pressure fluctuations near the front plate of the combustor are strongest and no spurious reflection at inlet and outlet radiation boundaries is observed. A stable solution of sound propagation with a mean flow field containing large density and flow field gradients is achieved by solving for the modified set of linearised Euler equations (12) to (14). Compared to the genuine linearised Euler equations, components consisting of mean-flow gradient terms are neglected, since they are potentially causing instabilities. Therefore, the use of a modified set of basic equations means a compromise between stability of the numerical simulation and the accurate depiction of sound refraction in the combustor.

Pressure spectra of the simulated operation case at the microphone position $z = 42.5\,\text{mm}$, $y = r = 42.5\,\text{mm}$, $x = h = 20\,\text{mm}$ are displayed in Figure 10. Numerical narrow band pressure spectra are evaluated from[68]

$$\hat{S} = \lim_{t\to\infty}\left[\frac{\hat{p}\hat{p}^*}{t}\right] \quad \text{and} \quad L_p = 10\log\left(\frac{\hat{S}\Delta f}{p_{ref}}\right) \tag{20}$$

with the reference pressure $p_{\text{ref}} = 2 \times 10^{-5}\,\text{Pa}$ and the frequency band $\Delta f = 1\,\text{Hz}$ in simulation and experiment. $\hat{p}$ and $\hat{p}^*$ denote harmonized acoustic pressure and its conjugate complex, respectively.

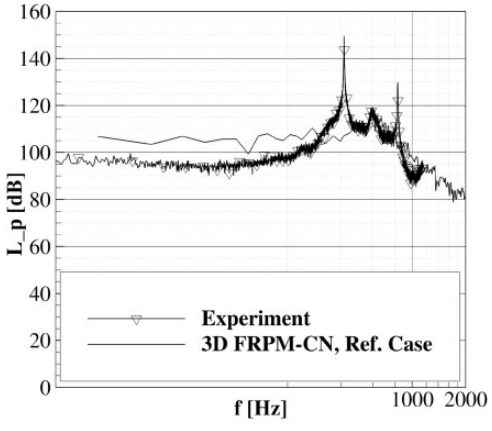

Figure 10. Comparison of experimentally (Stöhr and Werner, 2015, Personal communication) and numerically evaluated sound pressure spectrum[50] of the reference case in the combustion chamber at $z = 42.5\,\text{mm}$, $y = r = 42.5\,\text{mm}$, $x = h = 20\,\text{mm}$.

Experimental data show several distinct characteristics: Two peaks are present in the spectrum, assigned to a thermoacoustic instability with a longitudinal mode[69] at about 350–400 Hz. The second peak is assigned to its first harmonic at 650–800 Hz. In comparison, the numerical simulation with FRPM-CN has no distinct peak at the respective frequency positions, since thermoacoustic phenomena cannot be depicted with this hybrid, sequential method. Absolute noise levels are captured without altering turbulence quantities according to equation (16) or artificially scaling absolute sound pressure levels by changing the source variance in equation (17). Combustion noise levels are determined solely from CFD simulation input.

The FRPM-CN spectra show a very similar slope compared to the experimental spectrum for high frequencies. FRPM-CN indicates the fraction of direct combustion noise of the investigated operation point, due to the consideration of direct noise sources and sound propagation via linearised Euler equations only. The presented results therefore suggest that, in this particular case, direct combustion noise is dominant over indirect, since absolute sound pressure levels are fully reproduced with the employed broadband combustion noise simulation approach. This circumstance was confirmed by investigations on a different, swirl stabilized burner operated at atmospheric conditions.[49] Regions of potential indirect noise production, like the combustor exit area section, are modelled with steady background flow and unsteady sound propagation. Therefore, indirect noise is not resolved by the approach.

Additionally, there are discrepancies between numerical simulation and experimental pressure spectra. Especially for low frequencies, the characteristic tableau shape of the spectrum is reproduced by the simulation, but amplitudes are overestimated. As can be seen from fluctuating sound source signal at upstream and downstream observer points in Figure 16, downstream sources have a large amplitude and therefore a great influence on resulting sound pressure spectra. Due to larger timescales downstream in the shear layer, as indicated in Figure 15, downstream fluctuations are expected to rather contribute to the spectrum at lower frequencies. Therefore, a possible reason for discrepancies in this particular case is the inaccuracy of downstream turbulent timescale prediction by the CFD RANS simulation. As shown with the parametric study in Figure 12, the shape of pressure spectra could be slightly adapted by altering turbulent timescales. This however necessitates artificial amplitude scaling of sound source fluctuation in order to match experimental levels. Additionally, unwanted spurious noise could result from too coarse resolution of the sound source region, leading to poor quality of reconstructed profiles

and therefore variances of fluctuating synthetic sound sources. This circumstance is partially reflected in the variance profiles in Figures 13 and 14. A finer resolution of the source field grid would lead to a better representation of lengthscales from the CFD simulation in the combustion chamber and more accurate source filtering operations. A significant refinement however means a large increase of computational turnaround times and is therefore not considered in this work.

The computations were carried out in a total of 4052 CPU-h, while the CFD fraction of computational time amounts to 1356 CPU-h.

Further on, turbulence input for FRPM-CN is varied, based on the reference CFD simulation and according to Table 1. Turbulent integral length- and time scales serve as input for the stochastic sound source reconstruction algorithm, referring to equation (16).

Integral time scales are used for the synthetisation of turbulence-induced decay, while integral length scales determine local spatial source extensions. A variation of both is carried out in order to study the differences in spectral shape of combustion noise spectra in a complex, encased configuration dependent on different degrees of turbulence input.

Impact on pressure spectra from variation input of integral length-scales at the combustor microphone position $z = 42.5\,\text{mm}$, $y = r = 42.5\,\text{mm}$, $x = h = 20\,\text{mm}$ is studied in Figure 11. Combustion noise source spatial extensions are defined by the local integral length scale. An increase in turbulent length scales by larger values of $c_{T,l}$, as in Table 1 from Case 1 to Case 6 results in larger noise sources. Therefore, stronger forcing is applied and consequently overall noise levels are higher, as can be seen in Figure 11. However, no change in shape of spectra over the investigated frequency range is observed.

According to equation (17), a variation of integral time scales inversely affects sound source fluctuation amplitude. The larger integral time scales are used, the smaller absolute sound pressure levels in Figure 12 and vice versa. For a variation of integral time scales, however, a change of shape in combustion noise spectra in this particular case can be observed. The larger integral time scales are applied due to a variation of $c_{T,\tau}$ in equation (16), the more prominent low-frequency noise becomes. Further on, the slope of sound pressure spectra in Figure 12 for higher frequencies changes with variation of $c_{T,\tau}$. The descent in the spectra for higher frequencies becomes larger for larger values of $c_{T,\tau}$, as can be seen particularly for Cases 10 to 12. It would therefore be possible to achieve an improved match with experimental data compared to the results in Figure 10. However no calibration is carried out here. A fit of calibration constants would provide better agreement with measurements in this particular case. Then, for such a specific adaptation no general conclusion could be drawn for the applicability of FRPM-CN to different test cases. The carried out parametric variations indicate nonetheless, that there is only a weak correlation between a variation of turbulence related input and resulting sound pressure spectra.

Subsequently, reproduction ability of prescribed one- and two-point turbulence statistics with 3D FRPM-CN for the case without any scaling of turbulence quantities, $c_{T,l} = c_{T,\tau} = 1$, is analysed. Accordance of prescription and FRPM-CN reproduction of target variance on lateral profile lines and the quality of modelling of turbulence induced decay on

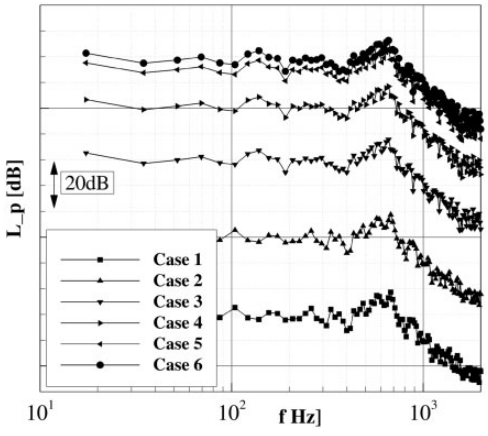

Figure 11. Variation of turbulent integral length scale input for FRPM-CN from CFD data, according to Table 1, impact on spectral shape of combustion noise for the PRECCINSTA burner test case.
CFD: computational fluid dynamics; FRPM-CN: fast random particle method for combustion noise.

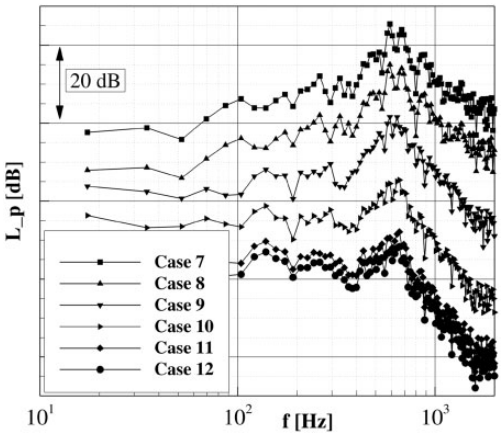

Figure 12. Variation of turbulent integral time scale input for FRPM-CN from CFD data according to Table 1, impact on spectral shape of combustion noise for the PRECCINSTA burner.
CFD: computational fluid dynamics; FRPM-CN: fast random particle method for combustion noise.

exemplary streamlines in the source domain close to the inner shear layer are investigated.

Local one-point statistics are reproduced for horizontal (Figure 13) and vertical profile lines (Figure 14) with almost identical quality, due to approximate rotational symmetry of the temperature variance profile in the combustor.

Positions of profile peaks are nicely reproduced in all horizontal profile lines. However, there is discrepancy in view of absolute values between target and numerical reproduction with 3D FRPM-CN. This is due to the employed Gaussian filter for sound source reconstruction which gives low peak values in case of local length scales being relatively large compared to variance profile extensions. Furthermore, filtering operations on basis of the local turbulent length scales from a spatial noise field results in blurred reproduced source variance profiles. Despite deviations in source fluctuation values, absolute combustion noise sound pressure levels are accurately predicted, as shown in Figure 10. This circumstance in view of rather poor representation of prescribed variance profiles upstream in the burner is assumed to be linked to discretisation of the source region and resulting weaknesses of the Gaussian filter leading to physical sound source extensions, as previously mentioned. As can be seen in Figures 13 and 14, reproductions are poor for upstream profiles, where variance profiles are narrow compared to lengthscales directly resolved by the source field grid. On the other hand, overall source field extensions are limiting the reconstruction of larger sources downstream. Those circumstances might lead to a certain fraction of unwanted noise production. The fact that absolute sound pressure levels are still well predicted in Figure 10 could be explained by, due to our experience, deviations in the reproduction of peak values does not have a significant impact on absolute amplitudes over a wide frequency range in the spectra, as long as broader regions are accurately reproduced.

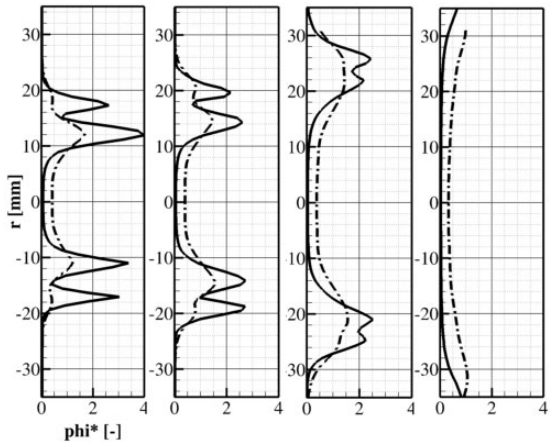

Figure 13. Exemplary prescribed and reproduced horizontal source variance profiles, reference case #1, profile lines at $h = 6$, 10, 20, 40 mm (left to right). Lines: statistical input, dash dotted: 3D FRPM-CN reproduction.
FRPM-CN: fast random particle method for combustion noise

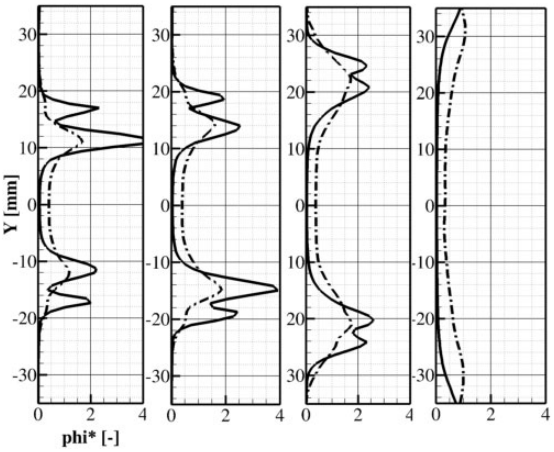

Figure 14. Exemplary prescribed and reproduced vertical source variance profiles, reference case #1, profile lines at $h = 6$, 10, 20, 40 mm (left to right). Lines: statistical input, dash dotted: 3D FRPM-CN reproduction.
FRPM-CN: fast random particle method for combustion noise

Over-prediction of reproduced variance levels in the inner recirculation zone close to the burner axis is due to large integral length-scales in the recirculation zones in the CFD simulation, which serve as criterion for local spatial source extensions. Furthermore, the prescribed variance according to e.g. equation (19) does not consider physical source extensions. It is a scalar estimation of source fluctuation intensity. The presence of local large length scales however leads to additional source contributions, especially in recirculation zones.

For the evaluation of turbulent decay synthetisation and therefore local 3D FRPN-CN two-point statistics reproduction ability, two different locations are investigated. Two-point correlation of transient source signal at 10 discrete points on an exemplary streamline according to Figure 8 is performed in the vicinity of the stagnation point of the swirled flow (C1) and once further downstream (C2) in the inner shear layer of the swirled flow. Properties of the investigated streamline and positions of carried out correlations are depicted in Figure 15. There, velocity, temperature variance and turbulence integral quantities and their development along the streamline are shown. For direct comparability, all variables are referenced to their maximum value. Normalized quantities are depicted over the number of discrete sampling points with an absolute spatial interval between points of $\Delta x = 0.83$ mm. For the cross-correlation in Figures 17 and 18, each fifth point is

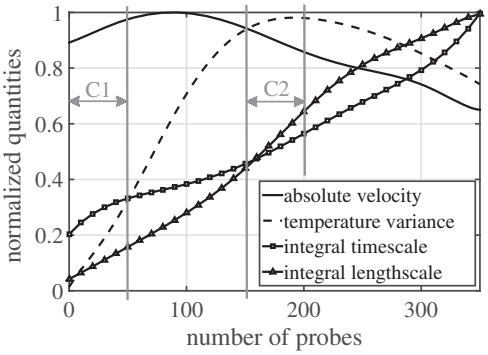

Figure 15. Normalized flow field, integral turbulence and temperature variance distribution along the selected streamline for cross-correlation analysis. C1 and C2 denote upstream (near-stagnation point) and downstream section for correlation analyses.

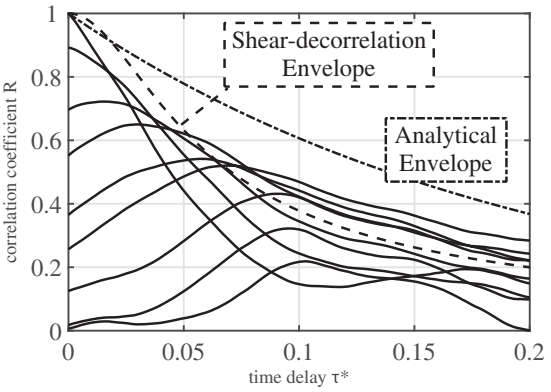

Figure 17. Source cross-correlation analysis for the reference case at exemplary streamline from Figure 8. Normalised cross-correlation coefficient over time-delay. Analytical envelopes with different degrees of decay of sources. Near stagnation point correlation C1.

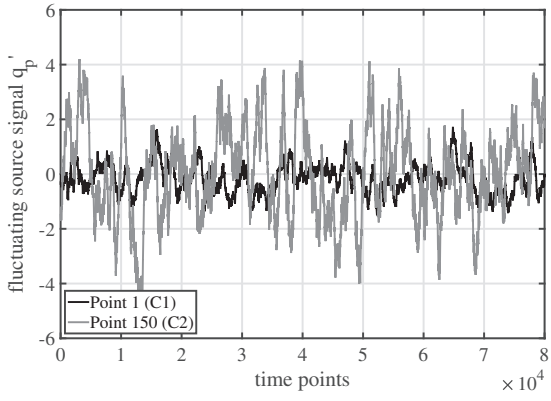

Figure 16. Normalized fluctuating sound source signal $q_p'/(f_{ref}\rho_{ref}c_{ref}^2)[-]$ at upstream points of respecting correlation sections C1 and C2 in Figure 15 over discrete time points.

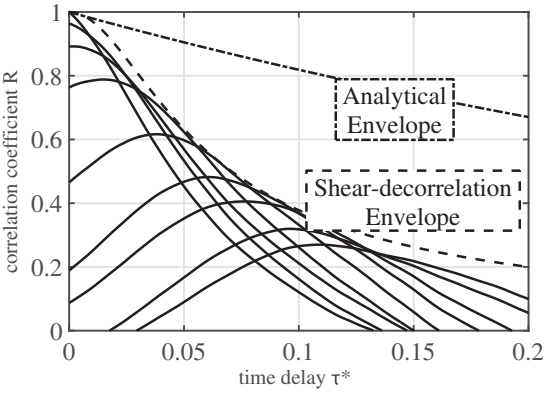

Figure 18. Source cross-correlation analysis for the reference case at exemplary streamline from Figure 8. Normalised cross-correlation coefficient over time-delay. Analytical envelopes with different degrees of decay of sources. Downstream correlation C2.

considered, leading to $\Delta x_{corr} = 3.32\,\text{mm}$. As can be seen in Figure 15, velocities first increase and then decrease along the streamline. Therefore, the streamline proceeds along the inner shear layer of the swirled flow from the probe number 100 approximately. As expected, turbulent scales increase continuously along the streamline.

Typical signals of fluctuating sound sources at the upstream points of cross-correlation sections C1 and C2 from Figure 15 are shown in Figure 16. Source fluctuation magnitude is considerably stronger at the downstream point (Point 150), compared to the upstream point (Point 1), since amplitude scaling due to the temperature variance distribution along the streamline is stronger downstream, as can be seen in Figure 15. Furthermore, fluctuations appear to be more small-scaled for the upstream point, as a consequence from smaller turbulent length-scales upstream. The impact of integral time scales can be clearly revealed from the following correlation only. Results of cross-correlation analysis are depicted in Figures 17 and 18.

A noticeable characteristic for both cross-correlation analyses in Figures 17 and 18 is the under-prediction of turbulent decay by the envelope of the first-order correlation model, evaluated with equation (5). The difference between analytical solution and numerical reproduction of the model correlation function can be explained with the effect of shear decorrelation, a phenomenon induced by the non-uniformity of the underlying mean flow field employed for source convection.

Shear decorrelation means an additionally induced decorrelation effect of sources due to velocity gradients normal to streamlines, along which combustion noise sound sources convect. This effect becomes relevant especially in the vicinity of the inner shear layer of

the swirled flow, where correlation analysis is carried out. There, velocity gradients normal to mean streamlines are large. An analytical envelope considering the effect of shear decorrelation can be described with[70]

$$R = \frac{1}{\sqrt{1 + 0.25\left(\frac{du}{dy}\right)^4 \tau^2}} \tag{21}$$

τ denotes the time-delay against which the numerical correlation is evaluated. du / dy is the velocity gradient normal to the streamline. It is estimated from CFD RANS averaged flow field data. For the herein carried out correlation analysis, the streamline-normal velocity gradient is set as constant for the respective correlation analysis along the streamline.

By comparison of upstream and downstream source signal cross-correlation in Figures 17 and 18 it is observed that the discrepancy of evaluated correlations to analytical envelope without shear-decorrelation effects is stronger for the downstream point. This indicates that shear decorrelation plays a bigger role for the downstream correlation section C2. This is consistent with the observations of Figure 15, since the streamline is located directly in the inner shear layer for correlation section C2 only. With the incorporation of shear-decorrelation effects according to equation (21), a good description of turbulence induced decay from the numerical simulation is achieved for similar normal-streamline velocity gradients du / dy. It however appears from the numerical evaluation of fluctuating source signal that both correlations feature a similar turbulence induced decay.

From the distribution of correlation peaks along the time delay axes in Figures 17 and 18 it can be inferred that the non-constant velocity distribution along the treated streamline is depicted, since their positions along the time-delay axis is not constant. Furthermore, correlation peaks of the downstream analysis in Figure 18 are wider, indicating that larger turbulent structures are depicted downstream, in accordance with the distribution of turbulent length scales in the combustor, where integral scales are larger further downstream close to the inner shear layer. Values for velocity and integral turbulent length scales are extracted from correlation analysis and the average CFD flow field are opposed in Tables 2 and 3. Reproduced velocity is evaluated from the ratio of monitoring point distance to downstream correlation peak position on the time delay axis. Locally reproduced length scales are estimated from fits of the analytical solution in equation (5) to downstream correlation peaks.

For both, upstream and downstream correlation analyses, there is a good representation of source convection by the numerical simulation ($u_{c,\mathrm{korr}}$), compared to the prescription from CFD simulations ($u_{c,\mathrm{CFD}}$). Maximum deviations are present at the downstream correlation section C2 for the most upstream point investigated. Besides this value, reproduced source convection velocities are in good agreement with CFD prescriptions, showing a maximum deviation of 0.1.

In terms of length scales, a good representation by the numerical simulation ($l_{T,\mathrm{korr}}$) can be observed for the downstream section C2 in Table 3 with larger length scales compared to the upstream section C1 in Table 2, with maximum deviations to the CFD input ($l_{T,\mathrm{CFD}}$) of about 0.324. However, significant differences between input and numerical realisation are present for the upstream correlation. The main reason for the upstream length scale deviations in Table 2 are suspected to be due to relatively small length scales close to the stagnation point. There, values of integral length scales are smaller than the direct grid resolution of

Table 2. Normalised correlation quantities at C1 for correlation peaks 5 to 8 from Figure 17.[a]

Point	$u_{c,\mathrm{korr}}$	$u_{c,\mathrm{CFD}}$	$(u_{c,\mathrm{korr}} - u_{c,\mathrm{CFD}})/u_{c,\mathrm{CFD}}$
P5	0.0564	0.05794	0.026
P6	0.0587	0.05841	0.005
P7	0.0547	0.05898	0.073
P8	0.0601	0.05954	0.009
Point	$l_{T,\mathrm{korr}}$	$l_{T,\mathrm{CFD}}$	$(l_{T,\mathrm{korr}} - l_{T,\mathrm{CFD}})/l_{T,\mathrm{CFD}}$
P5	0.005	0.00118	3.24
P6	0.0046	0.00126	2.65
P7	0.004	0.00142	1.82
P8	0.003	0.001523	0.97

[a]Normalisation quantities according to Appendix 1.

Table 3. Normalised correlation quantities at C2 for correlation peaks 5 to 8 from Figure 18.[a]

Point	$u_{c\mathrm{korr}}$	$u_{c\mathrm{CFD}}$	$(u_{c\mathrm{korr}} - u_{c\mathrm{CFD}})/u_{c\mathrm{CFD}}$
P5	0.0858	0.0619	0.39
P6	0.0677	0.0616	0.10
P7	0.0636	0.0612	0.04
P8	0.0604	0.0608	0.01
Point	$l_{T\mathrm{korr}}$	$l_{T\mathrm{CFD}}$	$(l_{T\mathrm{korr}} - l_{T\mathrm{CFD}})/l_{T\mathrm{CFD}}$
P5	0.0055	0.005986	0.081
P6	0.0045	0.006172	0.27
P7	0.0045	0.00644	0.301
P8	0.003	0.006661	0.324

[a]Normalisation quantities according to Appendix 1.

FRPM-CN. As a consequence, modelled sources appear larger than they should be according to the input definition. However as a compensation, their amplitude is downscaled according to the ratio of CFD length scales and the minimum value that is directly resolvable by FRPM-CN. This modelling strategy is implemented in order to conserve acoustic forcing as prescribed from CFD simulations. However, the discrepancy of small length scales from CFD and directly resolvable length scales can cause deviations of downstream source correlation peak extensions. Furthermore, errors appear to be large, however, upstream absolute length scale values are small for either prescription from CFD simulations and FRPM-CN reproduction.

Considering all carried out analyses for the FRPM-CN reproduction capability of local one- and two-point statistics, it can be stated that the method achieves a good representation of turbulence statistics. Nonetheless, there are certain deviations. From our experience, reducing the deviations can lead to a reduction of unwanted noise contributions and could therefore lead to a better agreement between experiment and numerical simulation in the comparison of Figure 10. For significant improvement of numerical reproduction, the source field grid of FRPM-CN would need refinement. Alongside, the number of particles necessary for noise generation would increase and thereby the computational time. Therefore, a sensible compromise has to be chosen for adequate source field resolution and turbulence statistics reproduction on the one hand, and, efficient combustion noise simulation with good agreement to experimental data at low computation costs on the other hand.

8 Conclusions

The hybrid, stochastic combustion noise prediction approach FRPM-CN was applied to the PRECCINSTA model combustor in view of applicability to a complex test case. The method relies on turbulence and flow field statistics as input for sound source reconstruction in the time domain. Sound propagation is realised with a modified set of linearised Euler equations, incorporating mean flow field information from CFD data. Resonance phenomena are theoretically detectable, while thermoacoustic cycles cannot be captured with a sequential, hybrid approach.

The stochastic ansatz reproduces turbulence induced decay based on integral length and time scale distribution in an assumed sound source region. The reproduction ability of local one- and two-point statistics was evaluated. It was shown that prescribed statistics were well captured and reproduced by FRPM-CN and that absolute sound pressure levels of combustion noise from experiments were accurately predicted, with some deviations in terms of integral turbulent length scale reproduction, limited to certain source field characteristics.

In the context of this particular application case it was stated that direct combustion noise is dominant over indirect in this encased, swirl stabilised combustion test case, since experimental pressure spectra were reproduced by an approach considering direct combustion noise sources in the reaction zone only.

Turbulence statistics input was varied for integral length and time scales and the impact on spectral shape and levels of combustion noise were analysed. It was found that combustion noise spectra are almost independent of variation of turbulence input for the PRECCINSTA burner test case in the investigated range. A change of spectral shape was shown to be achievable with a variation of turbulent integral time scale. However, no fitting of model constants was applied for the comparison with experimental data, in order to investigate the general applicability of the method in swirl stabilized combustion regimes.

Therefore, FRPM-CN was shown to serve as a robust and efficient tool for the analysis of combustion noise sound sources and pressure spectra. Combustion-induced noise source locations can be easily revealed. The fraction of direct combustion noise of overall acoustic pressure fluctuation in enclosed combustion systems with thermoacoustic phenomena can be reliably detected, relying on statistical input from steady-state CFD simulations only.

Acknowledgements

Dr Michael Stoehr and Stefanie Werner from the Combustion Diagnostics Department, Institute of Combustion Technology, DLR Stuttgart, are gratefully acknowledged for their provision of measured sound pressure spectra.

Declaration of Conflicting Interests

The author(s) declared no potential conflicts of interest with respect to the research, authorship, and/or publication of this article.

Funding

The author(s) received no financial support for the research, authorship, and/or publication of this article.

References

1. Leahy J. *Global market forecast 2015–2034, Presentation by John Leahy, Airbus Chief Operating Officer*. Available at: http://www.airbus.com/company/market/forecast/ (accessed March 2016).

2. Rolls-Royce. *The jet engine*. Birmingham: Renault Printing Co Ltd, Rolls-Royce plc, Derby, 1996. ISBN 10: 0902121235.
3. Leylekian L, Lebrun M and Lempereur P. An overview of aircraft noise reduction technologies. *Aerospace Lab J* 2014; 7: 1–15.
4. Dowling A and Mahmoudi Y. Combustion noise. *Proc Combust Inst* 2015; 35: 65–100.
5. Marble F and Candel S. Acoustic disturbance from gas non-uniformities convected through a nozzle. *J Sound Vib* 1977; 55: 225–243.
6. Cumpsty N and Marble F. Core noise from gas turbine exhaust. *J Sound Vib* 1977; 54: 297–309.
7. Cumpsty N and Marble F. The interaction of entropy fluctuations with turbine blade rows; a mechanism of turbojet engine noise. *Proc R Soc A* 1977; 357: 323–344.
8. Howe M. *Theory of vortex sound*. Cambridge: Cambridge University Press, 2003, ISBN: 0-521-81281-X.
9. Howe M. Indirect combustion noise. *J Fluid Mech* 2010; 659: 267–288.
10. Magri L, O'Brien J and Ihme M. Compositional inhomogeneities as a source of indirect combustion noise. *J Fluid Mech* 2016; 799: 1–12.
11. Leyko M, Nicoud F and Poinsot T. Comparison of direct and indirect combustion noise mechanisms in a model combustor. *AIAA J* 2009; 47: 2709–2716.
12. Tam C. On the spectrum of combustion noise. In: *21st AIAA/CEAS aeroacoustic conference*, Dallas, TX, USA, 22–26 June 2015.
13. Schuster B and Mendoza J. *Auxiliary power unit combustion noise measurements. X3-Noise/CEAS noise workshop*. Paper No. 2.
14. Miles J. Time delay analysis of turbofan engine direct and indirect combustion noise sources. *J Propul Power* 2009; 25: 218–227.
15. Hultgren L and Miles J. Noise source separation using internal and far-field sensors for a full-scale turbofan engine. AIAA 2009-3220.
16. Flemming F, Sadiki A and Janicka J. Investigation of combustion noise using a LES/CAA hybrid approach. *Proc Combust Inst* 2007; 31: 3189–3196.
17. Ihme M and Pitsch H. On the generation of direct combustion noise in turbulent non-premixed flames. *Int J Aeroacoust* 2012; 11: 25–78.
18. Bui T, Schröder W and Meinke M. Numerical analysis of the acoustic field of reacting flows via acoustic perturbation equations. *Comp Fluids* 2008; 37: 1157–1169.
19. Zhang F, Habisreuther P, Hettel M, et al. Numerical computation of combustion induced noise using compressible LES and hybrid CFD/CAA methods. *Acta Acust United Acust* 2012; 98: 120–134.
20. Brick H, Piscoya R, Ochmann M, et al. Prediction of the sound radiation from open flames by coupling a large eddy simulation and a kirchhoff method. *Acta Acust united Acust* 2005; 91: 17–21.
21. Andersson N, Eriksson LE and Davidson L. Large-eddy simulation of subsonic turbulent jets and their radiated sound. *AIAA J* 2005; 43: 1899–1912.
22. Lyrintzis A. Integral acoustics methods: from the (CFD) near-field to the (acoustic) far-field. *Int J Aeroacoust* 2003; 2: 95–128.
23. Silva C, Leyko M, Nicoud F, et al. Assessment of combustion noise in a premixed swirled combustor via large-eddy simulation. *Comp Fluids* 2013; 78: 1–9.
24. Liu Y, Dowling A, Swaminathan N, et al. Prediction of combustion noise for an aeroenginge combustor. *J Propul Power* 2014; 30: 114–122.
25. Hirsch C, Wäsle J, Winkler A, et al. A spectral model for the sound pressure from turbulent premixed combustion. *Proc Combust Inst* 2007; 31: 1435–1441.
26. Jörg C. *Experimental investigation and spectral modeling of turbulent combustion noise from premixed and non-premixed flames*. PhD Thesis, Lehrstuhl für Thermodynamik, Technische Universität München, 2015.
27. Liu Y and Echekki T. Modelling of combustion noise spectrum using temporal correlations of heat release rate from turbulent premixed flames. In: *21st AIAA/CEAS aeroacoustics conference*, AIAA 2015-2970, Dallas, TX, USA, 22–26 June 2015.
28. Liu Y, Dowling A, Swaminathan N, et al. Spatial correlation of heat release rate and sound emission from turbulent premixed flames. *Combust Flame* 2012; 159: 2430–2440.
29. Kotake S and Takamoto K. Combustion noise: effects of the shape and size of burner nozzle. *J Sound Vib* 1987; 112: 345–354.
30. Kotake S and Takamoto K. Combustion noise: effects of the velocity turbulence of unburned mixture. *J Sound Vib* 1990; 139: 9–20.
31. Rajaram R and Lieuwen T. Acoustic radiation from turbulent premixed flames. *J Fluid Mech* 2009; 637: 357–385.
32. Mahan J and Karchmer A. Combustion and core noise. *Aeroacoust Flight Veh* 1991; 1: 483–517.
33. Tam C, Golebiowski M and Seiner J. On the two components of turbulent mixing noise from supersonic jets. In: *2nd AIAA/CEAS aeroacoustic conference*. AIAA 1996-1716, Hampton, VA, USA, 24–26 March 1975.
34. Tam C, Pastouchenko N, Mendoza J, et al. Combustion noise of auxiliary power units. AIAA 2005-2829.
35. Mathews D and Rekos N Jr. Prediction and measurement of direct combustion noise in turbopropulsion systems. *J Aircraft* 1977; 14: 850–859.
36. Ho P and Doyle V. Combustion noise prediction update. In: *5th aeroacoustics conference*. AIAA paper 79-0588.
37. Mühlbauer B, Ewert R, Kornow O, et al. Simulation of combustion noise using CAA with stochastic sound sources from RANS. In: *14th AIAA/CEAS aeroacoustic conference*, AIAA 2008-2944, Vancouver, British Columbia, Canada, 5–7 May 2008.
38. Ewert R and Emunds R. CAA slat noise studies applying stochastic sound sources based on solenoidal digital filters. In: *11th AIAA/CEAS aeroacoustics conference*, AIAA 2005-2862, Monterey, CA, USA, 23–25 May 2005.
39. Ewert R. Slat noise trend predictions using CAA with stochastic sound sources from a random particle-mesh method (RPM). In: *12th AIAA/CEAS aeroacoustics*

conference. AIAA 2006-2667, Cambridge, MA, USA, 8–10 May 2006.
40. Ewert R. RPM – the fast random particle-mesh method to realize unsteady turbulent sound sources and velocity fields for CAA applications. In: *13th AIAA/CEAS aeroacoustics conference*, AIAA 2007-3506, Rome, Italy, 21–23 May 2007.
41. Ewert R. Broadband slat noise prediction based on CAA and stochasic sound sources from a fast random particle-mesh (RPM) method. *Comp Fluids J* 2008; 37: 369–387.
42. Mühlbauer B, Ewert R, Kornow O, et al. Evaluation of the RPM approach for the simulation of broadband combustion noise. *AIAA J* 2010; 48: 1379–1390.
43. Candel S, Durox D, Ducruix S, et al. Flame dynamics and combustion noise: progress and challenges. *Int J Aeroacoust* 2009; 8: 1–56.
44. Grimm F, Ewert R, Dierke J, et al. The fast random particle method for combustion noise prediction. In: *20th AIAA/CEAS aeroacoustics conference*, AIAA paper 2014-2451, Atlanta, GA, USA, 16–20 June 2014.
45. Grimm F, Ewert R, Dierke J, et al. Broadband combustion noise prediction with the fast random particle method. In: *Proceedings of ASME turbo expo 2014*, GT2014-25195, Duesseldorf, Germany, 16–20 June 2014.
46. Grimm F, Ewert R, Dierke J, et al. Efficient full 3d turbulent combustion noise simulation based on stochastic sound sources. In: *21st AIAA/CEAS aeroacoustics conference*, AIAA paper 2015-2973, Dallas, TX, USA, 22–26 June 2015.
47. Ewert R, Dierke J, Siebert J, et al. CAA broadband noise prediction for aeroacoustic design. *J Sound Vib* 2011; 330: 4139–4160.
48. Grimm F, Reichling G, Ewert R, et al. Efficient combustion noise simulation of a gas turbine model combustor based on stochastic sound sources. In: *Proceedings of ASME turbo expo 2015*, GT2015-42390, Montreal, Canada, 15–19 June 2015.
49. Grimm F, Reichling G, Ewert R, et al. Stochastic and direct combustion noise simulation of a gas turbine model combustor. *Acta Acust united Acust* 2017; 103: 262–275.
50. Grimm F, Ohno D, Noll B, et al. Broadband combustion noise simulation of the PRECCINSTA burner based on stochastic sound sources. *J Eng Gas Turbines Power* 2017; 139: 011505–011505–10. (GTP-16-1254.
51. Pope S. *Turbulent flows*. Cambridge, UK: Cambridge University Press, 2000.
52. Lighthill M. On sound generated aerodynamically. i. General theory. *Proc R Soc* 1952; A 211: 564–587.
53. Lighthill M. On sound generated aerodynamically. ii. Turbulence as a source of sound. *Proc R Soc* 1954; A 222: 1–32.
54. Tam C and Auriault L. Jet mixing noise from fine-scale turbulence. *AIAA J* 1999; 37: 145–153.
55. Mühlbauer B, Ewert R, Kornow O, et al. Numerical simulation of broadband combustion noise with the RPM-CN approach. In: *Proceedings of ASME turbo expo 2009*, GT2009-59870, Orlando, Florida, USA, 8–12 June 2009.
56. Mühlbauer B, Ewert R, Kornow O, et al. Numerical simulation of broadband combustion noise based on stochastic source reconstruction. In: *16th international congress on sound and vibration*, Krakow, Poland, 5–9 July 2009.
57. Ewert R, Dierke J, Pott-Pollenske M, et al. CAA-RPM prediction and validation of slat setting influence on broadband high-lift noise generation. In: *16th AIAA/CEAS aeroacoustics conference*, AIAA 2010-3833, Stockholm, Sweden, 7–9 June 2010.
58. Mühlbauer B. *Numerische simulation von verbrennungslärm*. PhD Thesis, Institut für Verbrennungstechnik der Luft- und Raumfahrt, Universität Stuttgart, 2012. http://elib.uni-stuttgart.de/opus/volltexte/2012/7137/ (accessed March 2016).
59. Menter F, Kuntz M and Langtry R. Ten years of industrial experience with the SST turbulence model. In: Hanjalic K, Nagano Y and Tummers M (eds) *Turbulence, heat and mass transfer*, 4th ed. Danbury, CT, USA: Begell House, Inc, 2003, pp.625–632.
60. Gerlinger P. *Numerische verbrennungssimulation – effiziente numerische simulation turbulenter verbrennung*. Germany: Springer-Verlag, 2005. ISBN 3-540-23337-7.
61. Dem C, Stöhr M, Arndt C, et al. Experimental study of turbulence-chemistry interactions in confined swirl flames with different degrees of premixing. *Z Phys Chem* 2015; 229: 569–585.
62. Oberleithner K, Stöhr M, Im S, et al. Formation and flame-induced suppression of the precessing vortex core in a swirl combustor: experiments and linear stability analysis. *Combust Flame* 2015; 162: 3100–3114.
63. Westbrook C and Dryer F. Simplified reaction mechanisms for the oxidation of hydrocarbon fuels in flames. *Combust Sci Technol* 1981; 27: 31–43.
64. Delfs J. *Basics of aeroacoustics, lecture notes*. Braunschweig, DLR – German Aerospace Center, Braunschweig, Germany, 2008.
65. Tam C and Webb J. Dispersion-relation-preserving finite difference schemes for computational acoustics. *J Comput Phys* 1993; 107: 262–281.
66. Krige D. A statistical approach to some basic mine valuation problems on the witwatersrand. *J Chem Metal Min Soc S Afr* 1951; 52: 119–139.
67. Tam C and Dong Z. Wall boundary conditions for high-order finite-difference schemes in computational aeroacoustics. *Theor Comput Fluid Dyn* 1994; 6: 303–322.
68. Ewert R, Appel C, Dierke J, et al. Rans/caa based prediction of naca 0012 broadband trailing edge noise and experimental validation. In *15th AIAA/CEAS aeroacoustics conference*, AIAA 2009-3269, Miami, Florida, USA, 11–13 May 2009.
69. Lourier JM. *Numerische Simulation von thermoakustischen Instabilitäten in Gasturbinenbrennkammern mithilfe von Impedanzrandbedingungen*. PhD Thesis, Institut für Verbrennungstechnik der Luft- und Raumfahrt, Universität Stuttgart, 2015.
70. Dierke J, Appel C, Siebert J, et al. 3d computation of broadband slat noise from swept and unswept high-lift wing sections. In: *17th AIAA/CEAS aeroacoustics conference (32nd AIAA aeroacoustics conference)*, Portland, Oregon, USA, 5–8 June 2011. DOI: 10.2514/6.2011-2905.

Appendix 1

Notation

$\hat{A}$	amplitude function	–
c_p	specific heat capacity	J/kg K
c_{Tl}	scaling constant, turb. length scale	–
$c_{T\tau}$	scaling constant, turb. time scale	–
C_T	dissipation model constant	–
D	characteristic tube diameter	m
f	frequency	Hz
f	mixture fraction	–
$\hat{G}_a$	adjoint Green's function	–
$\mathcal{G}$	spatial filter kernel	–
i	imaginary unit	–
k	turbulent kinetic energy	m^2/s^2
l_T	integral length scale	m
L_p	sound pressure spectrum	dB
$\mathcal{L}$	Wave equation operator	–
$\dot{m}$	mass flow rate	kg/s
Ma	Mach number ($\lvert\widetilde{\boldsymbol{u}}\rvert/\sqrt{\gamma R_s \overline{T}}$)	-
n	spatial dimension	–
$\bar{p}$	mean pressure	Pa
p'	acoustic pressure	Pa
Pr	Prandtl number ($\mu c_p/\lambda_t$)	–
Pr_t	turbulent Prandtl number ($\mu_t c_p/\lambda$)	–
P_{th}	thermal load	W
q	general source term	Pa/s
q_p	combustion noise source term	Pa/s
Q	general source term	–
$\boldsymbol{r}$	spatial separation	m|m|m
r_i	random value of particle i	–
R	decorrelation envelope	–
$\mathcal{R}$	cross-correlation coefficient	–
$\hat{R}$	variance of a correlated variable	K^2/s^2
Re	Reynolds number ($\rho\widetilde{\mathrm{l}}uD/\mu$)	–
R_s	specific gas constant	J/(kg K)
s_i	fraction of random value of particle i	–
$\hat{S}$	power spectral density	dB/Hz
t	time	s
t_{I}	integration time	s
$\tilde{T}$	Favre averaged temperature	K
T''	fluctuating temperature	K
T''^2	temperature variance	K^2
$\widetilde{\boldsymbol{u}}_0^c$	average velocity from RANS	m/s|m/s|m/s
$\widetilde{\boldsymbol{u}}$	Favre averaged velocity	m/s|m/s|m/s
$\widetilde{\boldsymbol{u}}'$	acoustic velocity	m/s|m/s|m/s
$\mathcal{U}$	white noise field	–
V_S^n	source field volume, dimension n	m^2, m^3
$\boldsymbol{x}$	source field coordinates	m|m|m

$\boldsymbol{x}_{\mathrm{I}}$	far-field observer coordinates	m|m|m
$\boldsymbol{x}'$	auxiliary coordinates	m|m|m
α	Langevin model constant	–
β	Langevin model constant	–
β^*	turbulence model constant	–
γ	isentropic exponent	–
δ	dirac function	–
Δ	difference	–
λ	thermal heat conductivity	W/(mK)
μ	dynamic viscosity	kg/(ms)
μ_t	turbulent dynamic viscosity	kg/(ms)
ξ	Gaussian distributed noise forcing	–
ρ	density	kg/m^3
ρ'	fluctuating density	kg/m^3
$\bar{\rho}$	averaged density	kg/m^3
τ	time delay, temporal separation	Σ
τ_T	integral time scale	Σ
φ	effective source std. dev.	Pa/s
Φ	equivalence ratio	–
ω	circular frequency	$H\zeta$
ω	turbulence frequency	$H\zeta$

Reference conditions

Reference conditions for normalisation of CFD quantities in the CCA simulations are evaluated from ambient upstream air plenum conditions for air at $T = 320\,\mathrm{K}$. They are given in the following:

c_{ref}	speed of sound	358.5 m/s
f_{ref}	frequency	358.5 Hz
l_{ref}	reference length	1 m
R_{s}	specific gas constant	287.058 J/(kg K)
γ_{ref}	isentropic exponent	1.4
μ_{ref}	dyn. viscosity	$17.1 \cdot 10^{-6}\mathrm{Pa} \cdot \mathrm{s}$
ρ_{ref}	density	$1.1\,\mathrm{kg/m^3}$